

# Acquisition and Application of Reflectance for Computer-Generated Images: A Critical Review

Belinda Emmily Tepper, Royal Melbourne Institute of Technology, Australia\*

 <https://orcid.org/0009-0002-5350-9161>

Benjamin Francis, Australian Defence, Australia

Lijing Wang, Royal Melbourne Institute of Technology, Australia

 <https://orcid.org/0000-0002-7300-9271>

Bin Lee, Australian Defence, Australia

## ABSTRACT

In the field of computer graphics, accurate representation of material properties is crucial for rendering realistic imagery. This paper focuses on the bidirectional reflectance distribution function (BRDF) and its role in determining how materials interact with light. The authors review the state of the art in reflectance measurement systems, with a focus on BRDF and bidirectional texture function (BTF) measurement. They discuss practical limitations in measuring multi-dimensional functions and provide examples of how researchers have addressed these challenges. Additionally, they analyse various approaches to converting measured data into practical analytical functions for use in commercial rendering software, including data-driven methods such as neural networks and hybridized approaches.

## KEYWORDS

BRDF, BTF, Computer Graphics, Reflectance Measurement

## 1. BACKGROUND

Reflectance functions are used to describe the transport of light from the illumination direction to the viewing direction. Ideally, a reflectance function is a model of how a particular surface should look under all possible lighting conditions and all viewing angles. The BRDF (Nicodemus et al., 1977) is important for rendering realistic computer graphics imagery, as it serves as a predictive model of the appearance of materials. The model aims to predict the scattering of electromagnetic energy based on the composition of the material. An idealized model would encompass all the qualities necessary to describe shiny metals, rough dielectrics, and soft, translucent materials in high fidelity, subjectively appearing photo-realistic to the viewer. Analytically derived models are based on approximations and assumptions. Initially, the models were relatively simple functions with a small number of parameters describing the light transport to reduce the impact of computation resources.

DOI: 10.4018/IJCVIP.331386

\*Corresponding Author

This article published as an Open Access article distributed under the terms of the Creative Commons Attribution License (<http://creativecommons.org/licenses/by/4.0/>) which permits unrestricted use, distribution, and production in any medium, provided the author of the original work and original publication source are properly credited.

These reflectance models, therefore, are evaluated in terms of the efficiency and accuracy of the model's prediction. Contemporary graphics are more demanding, and data driven approaches have been increasingly relied upon, evaluating how well an analytical model compares to real world data. However, capturing data is a lengthy procedure to document multiple dimensions of a reflectance function, and no agreed standards exist for data acquisition. Many unique designs have been purposely built and tested using novel techniques that aim to capture the data in the most efficient manner, whilst retaining high density.

This paper reviews the state of the art in reflectance capture and presents to the reader different categories of devices demonstrating their strengths and weaknesses. The methodology of fitting the data to analytical reflectance functions is also explored. Studies used in the development of commercial renderers are discussed, and a selection of contemporary fitting metrics are introduced.

To describe the complete interaction of the surface with electromagnetic energy, a significantly complex and higher dimension function is required, but it is impractical to measure or render. As many as 14 dimensions of the scattering function,  $SF(x_i, y_i, z_i, \theta_i, \phi_i, \lambda_i, t_i, x_o, y_o, z_o, \theta_o, \phi_o, \lambda_o, t_o)$ , must be considered. These are the position  $x$ ,  $y$ , and  $z$ , angles  $\theta$ , and  $\phi$ , wavelength  $\lambda$ , time  $t$ , a distribution of light reaching a surface and the position, angle, wavelength, and time of the same distribution leaving the surface. Further dimensions are also possible including the polarized state, and temperature, *esp.* with regards to infrared frequencies.

Some subsets of the scattering function apply to specific types of surfaces, such as the 6 dimensional spatially varying bidirectional reflectance distribution function,  $SVBRDF(x_i, y_i, \theta_i, \phi_i, \theta_o, \phi_o)$ , for measuring reflectance of a non-uniform surface profile, *i.e.* a surface which exhibits irregularities. In practice, this is often a planar area measurement of an area  $xy$  for the incoming irradiance and outgoing reflectance direction, which is commonly referred to as the Bidirectional Texture Function (BTF). (Dana et al., 1999) A typical example is textiles that have an arrangement of fibers in some regular pattern.

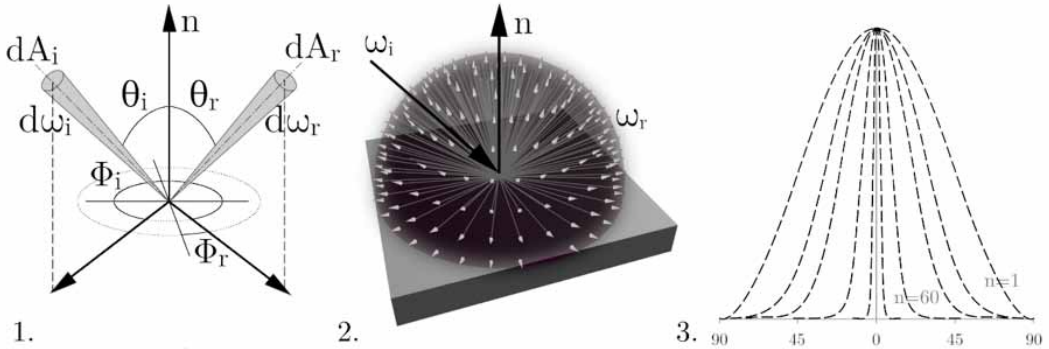
Subsurface scattering is particularly useful for characterizing surfaces, such as skin or wax, that have a softened appearance. The 8D bidirectional sub-surface scattering reflectance distribution function,  $BSSRDF(x_i, y_i, \theta_i, \phi_i, x_o, y_o, \theta_o, \phi_o)$ , may be used for measuring such surfaces where light entering at one point scatters under the surface, and then exits the again at a macro scale distance. (Weyrich et al., 2009) In many practical applications, however, the BRDF, a 4D function that considers the reflectance of a uniform surface, is considered a sufficient approximation. The BRDF formulation, first described by Nicodemus (1977), is a reflectance function  $f_r$ , as shown in *Equation 1*, of the incoming irradiance incident at a single point on the surface and the outgoing radiance from the point leaving the surface in the viewing direction, shown in *Figure 1-1*. This can be used to characterise many common dielectrics such as plastic, ceramic or paper, and most homogeneous metallic surfaces.

$$f_r(\theta_i, \phi_i; \theta_r, \phi_r) = \frac{\omega_r(\theta_r, \phi_r)}{\omega_i(\theta_i, \phi_i) \cos \theta_i d\omega_i} \quad (1)$$

BRDF measurement must consider at least four parameters representing these dimensions, the irradiance  $\omega_i$ , the exiting radiance  $\omega_r$ , the azimuth angle  $\phi$ , and the zenith angle  $\theta$ , as shown in *Equation 1*. The BRDF function also observes properties of reciprocity of the directions, known as Helmholtz reciprocity, whereby the incoming and outgoing directions may be reversed ( $f_r(\omega_o, \omega_i) = f_r(\omega_i, \omega_o)$ ), and bilateral symmetry. Reciprocity, and energy conservation are often used to evaluate whether an analytical model has a plausible physical basis.

Many real surfaces may be described by a BRDF function, providing the reflectance is localized, having limited internal interactions. Perfect specular distributions for example, describe mirror-like

Figure 1. (1) The bidirectional reflectance distribution function showing the solid angles of incoming and outgoing direction; (2) the Lambertian diffusion model; (3) specular lobe slices of the Blinn-Phong model for values of slope  $n$  ( $n=1,5,10,60,1200$ ) (Akenine-Moller et al., 2008)



surfaces, such as polished metals, where all the light hitting the plane is reflected in a single mirror direction. When a material is perfectly specular the angle  $\theta$  between the incident ray  $\omega_i$  and the normal  $N$  is the same as the outgoing ray  $\omega_r$  in the opposite direction. Likewise, idealized diffuse surfaces, such as velvet, matte painted finishes, or snow, describe a type of surface where the reflected light is the same intensity in all directions. The Lambertian reflectance distribution, which describes these surfaces, observes that for light hitting a diffuse object, the distribution is isotropic and the luminous intensity is a function of the cosine of the angle  $\theta$  between the surface normal  $N$  and the light direction  $\omega_i$ , shown in Equation 2 and Figure 1-2. Most physical surfaces are not perfect reflectors however, and only some of the light is reflected, whereas, the remaining portion is absorbed or transmitted. This ratio of absorption and reflection is described as the albedo  $\rho$  of the surface.

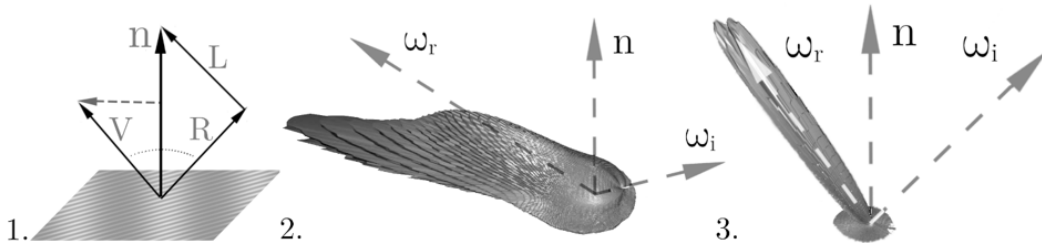
$$f_{diffuse} = N \cdot L = \cos \theta \quad (2)$$

When the surface does not exhibit perfect mirror or matte reflectance, the BRDF is an important and useful description of the weighting of energy on the surface consisting of these two components, the specular reflection component, and the diffuse component. Most analytical BRDF models generalize the reflectance distribution function to some parameters that describes the surface reflectance detailed below. For this reason, these models exhibit inherent inaccuracies. Often, this approximation has served the purpose well, where a high degree of accurate representation is not required and computing resources are constrained.

The Phong (1975) model (or Phong shader), for example, is a lightweight approximation and was previously frequently used in real time graphics applications. The model interpolates a flat shaded model (Gouraud shading), making assumptions about the orientation of the normals, to approximate the diffuse component of the material (Figure 1-3). Additionally, a specular lobe is applied as an empirical approximation of the reflectance of the material (Phong, 1975). This specular component is based on the empirical values of  $n$  and  $K$ , where  $n$  is a power of the specular function and  $K_s$  is the spread or intensity of the specularity, as shown in Equation 3 and illustrated in Figure 2.

$$f_r = K_d * f_{diffuse} + K_s * f_{specular} = K_d (N \cdot L) + K_s (V \cdot R)^n \quad (3)$$

Figure 2. (1) The geometrical relationship of Phong reflectance (Blinn, 1977).  $V$  is the viewing direction and  $R$  ( $R = 2(N \cdot L) N - L$ ) is the true mirror reflection direction. 2-3. Measured BRDFs showing the specular and diffusion spread of the lobes. (2) Cardboard that exhibits a mostly diffuse profile. Note that few diffuse profiles entirely conform to Lambertian reflectance even when there is no apparent specularly, (3) painted metal. The significant specular portion is apparent in the reflection direction while the diffusion part is small.



Simple empirical models like the Phong shader do not model the physical characteristics of light, however. Therefore, the goal of contemporary physical based rendering (PBR) is to approximate reflectance by satisfying three conditions, 1) it uses a micro-faceted model, 2) it should conserve energy, and 3) it uses an analytical, physical-based BRDF. A conceptual understanding of fitting to a physically-based material can be attained by holding the incoming ray direction  $\omega_i$  constant and observing all the outgoing directions  $\omega_r$ , or a slice of  $\omega_r$  which is plotted to a 2d graph. The diffuse component is the hemispherical shape at the center, shown in the two examples of Figure 2-2 and Figure 2-3. The elongated/ellipsoidal spur represents the specular component, known as the reflectance lobe. The lobe will tend towards the reflection direction of the incoming ray. Thin “sharp” lobes represent sharper reflectance, whereas wider lobes describe some surface roughness.

Physical-based representations, such as the Cook-Torrance (1982) model, attempt to model the physical surface characteristics of the material. The Fresnel reflectance of the material assumes a very flat surface must exist close to the optical flatness of the wavelength under investigation. The Cook-Torrance model, therefore, surmises that for a roughened surface, some micro-structure must also exist, and this surface must be a series of micro-facets resembling the required flatness for Fresnel reflectance to occur. The roughness of a surface is a statistical approximation of these micro-facets facing a certain direction, the directional distribution, based on a roughness parameter  $\alpha$ . These can be conceptualized as theoretical normal vectors clustered around the true reflectance normal which gives rise to the shape of the specular lobe. The ratio of the alignment of the micro-facets to the half vector  $h$  defines the roughness of the surface. This half vector, illustrated in Figure 3-1, is the unit vector that is halfway between the incident and viewing angle of the micro-facet calculated as the sum of the incident and viewing angle divided by its length, shown in Equation 4 (Blinn, 1977).

$$h = \frac{\omega_i + \omega_r}{\|\omega_i + \omega_r\|} \quad (4)$$

The micro-structure surface is approximated mathematically by three important parameters, which determines the fidelity of the Cook-Torrance analytical BRDF model. These three terms are the roughness term  $D$ , the shadowing term  $G$ , and the Fresnel term  $F$ . The  $D$  term, describes the probability of facets facing the half angle  $h$ . The  $D$  may be represented, as per the originally postulated model, using either the Beckmann distribution shown in Equation 5 or the Gaussian distribution function as described by Blinn (1977), shown in Equation 6, where  $c$  is a constant value.

$$D = \frac{1}{m^2 \cos^4 \alpha} e^{-\frac{\tan(\alpha)^2}{m}} \quad (5)$$

$$d = ce^{-\frac{\alpha^2}{m}} \quad (6)$$

The value of  $m$  in Equations 5 and 6 describes the arrangement of the facets on the surface. Small values of  $m$  describe a specular point, which is due to the highly directional nature of the reflectance. Large values of  $m$  describe a spread out (roughly Gaussian) specular component. This has a direct relationship with the sharpness of the specular peak, as shown in Figure 3-2 and Figure 4-1. Hence, on very rough surfaces, we would expect to find random alignment and a diffuse surface profile.

As with all outgoing radiance, each micro-surface has a projected area. Figure 4-2 shows the weighting of the individual facets in terms of their projected area (Heitz, 2014). This is the primary reason behind the geometric attenuation factor  $G$  shown in Equation 7, as the purpose of this function is to describe how much light is attenuated by the solid angle in the viewing direction, as compared to the normal direction.

$$G = \min \left\{ 1, \frac{2(n \cdot h)(n \cdot \omega_r)}{\omega_r \cdot h} \frac{2(n \cdot h)(h \cdot \omega_i)}{(\omega_r \cdot h)} \right\} \quad (7)$$

How the light arrives at and exits the surface, based on the surface profile of the micro-facets, is also somewhat critical to understanding the accuracy of the approximation of a real surface. As illustrated in Figure 5, a facet may be masked or shadowed, according to the geometry. The light may

Figure 3. (1) Different values of roughness modeled on the surface of a sphere ( $m$  roughness: 1.0, 0.8, 0.6, 0.4, 0.2, 0.0); (2) Cook-Torrance geometry of reflection with respect to the half vector as introduced by Blinn

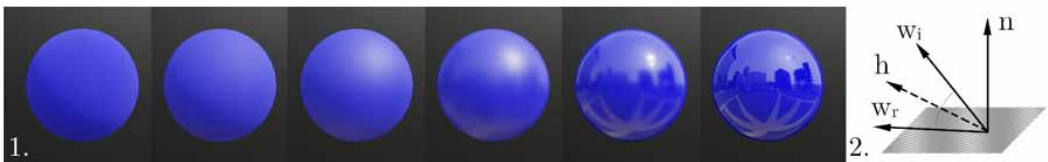


Figure 4. (1) The specular lobes for different values of  $m$  ( $m=0.1, m=0.25$ ), similar to those described in the paper by Cook and Torrance (1982); (2) the project area  $A$  of each micro-facet in the viewing direction; (3) lobe fitting to a BRDF profile (blue), three specular lobes are used (red), in this case, in addition to a diffuse lobe (center green) (Nguyen, 2008)

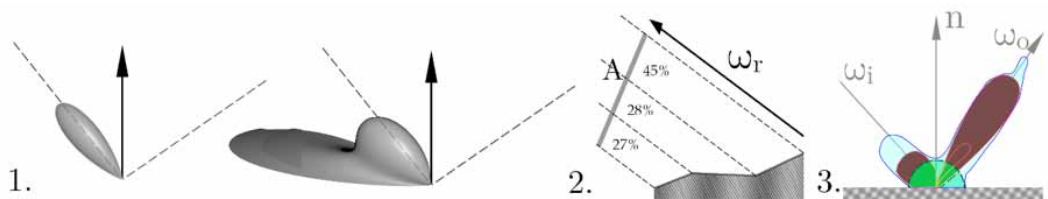
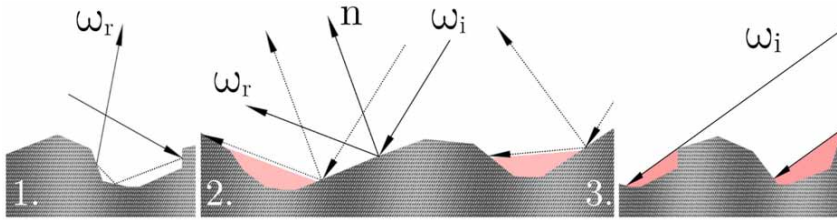


Figure 5. Different interactions of light with the micro-surface: (1) shadowing, (2) masking, and (3) inter-reflections



also undergo an indirect route before exiting, known as inter-reflection. This latter phenomenon is often not well modeled in parametric BRDFs.

A material Fresnel value  $F$  should be measured where practical due to the complexity of solving for the Fresnel equations directly. This Fresnel measurement taken implies a polished surface and is, therefore, multiplied by  $1/\pi$  to obtain bidirectional reflectance for a rough surface. The generalized form of the micro-faceted model for isotropic materials is shown in Equation 8 (Cook & Torrance, 1982) (Burley, 2012).

$$f_r(\omega_i, \omega_o) = k_d f_{diffuse} + k_s f_{specular} = k_d \frac{c_{diff}}{\pi} + \frac{F(\theta_d) D(\theta_h) G(\theta_i, \theta_v)}{4 \cos \theta_i \cos \theta_v} \quad (8)$$

More complex interactions of the subsurface are not considered by the micro-faceted model, which lacks the power to describe the light exiting beyond a localized distance. Yet, these interactions are important for modeling certain materials, *esp.* biological surfaces such as skin and leaves which are layered surface structures.

In practice, many theoretical functions have been postulated for the terms  $F$ ,  $D$ , and  $G$  since the original model was published, and the *Data fitting* section discusses these further. Table 1 lists some analytical, micro-facet BRDF models, though they do not expressly use these terms, but are nevertheless based on physical approximations. Ward (1992) expresses the distribution as anisotropic components  $\alpha_x$  and  $\alpha_y$ . Oren-Nayar (1994) present a more physically accurate diffuse only model accounting for inter-reflections (the Lambertian model holds when *roughness*=0). Lafortune (1997) gives a compact model consisting of lobes which are capable of representing phenomenon such as off-specular peaks and retro-reflection, and the Ashikhmin-Shirley (2000) model, which like Ward, models anisotropic directions denoted in the table as  $\alpha_x$  and  $\alpha_y$ . For a more comprehensive BRDF analytical model review consult Montes and Ure (Soldado & Almagro, 2012).

The BRDF is a subset of bidirectional functions that attempt to describe the surface. Variation over the surface can also cause the BRDF to become an inaccurate representation as the function assumes a uniform surface profile. Additionally, many surfaces are not well modeled by a single reflectance lobe, primarily due to off-specular (see Figure 4-3). In many cases this may be due to the materials which are layered, or composite, or to describe a retro-reflective peak. Therefore, the BRDF may be a sum of the fitted lobes at the expense of efficiency.

## 2. MEASUREMENT SYSTEMS OF REAL REFLECTANCE

While many purely analytical BRDF models may be conveniently formulated from optical principles, measuring the BRDF in laboratory settings is known to be a problematic exercise and incurs all the common pitfalls of an optical system. Rusinkiewicz (1997) noted numerous problems in conventional measurement, partially owing to the difficulty of measuring the 4 dimensions, shown in Equation 1.

Table 1. An overview of some analytical, micro-facet BRDF models

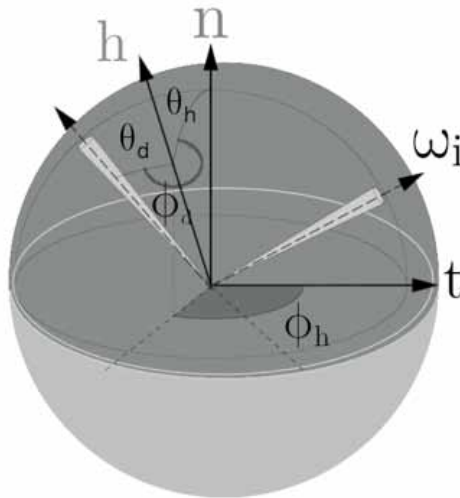
Model	Function	Comments
1. Ward (1992)	$f_r(\omega_i, \omega_o) = \frac{p_d}{\pi} + \frac{p_s}{4\pi\alpha_x\alpha_y\sqrt{\cos\theta_i\cos\theta_o}} e^{-\tan^2\theta_h} \left( \frac{\cos^2\phi_h}{\alpha_x^2} + \frac{\sin^2\phi_h}{\alpha_y^2} \right)$	Has both an isotropic and anisotropic model which includes the directions $\alpha_x$ and $\alpha_y$
2. Oren-Nayar (1994)	$f_r(\omega_{i,o}) = \frac{p_d}{\pi} E_o \cos\theta_i \left( A + B \max\left(0, \cos(\phi_o - \phi_i) \sin\alpha \tan\beta\right) \right)$ $A = 1.0 - 0.5 \frac{\sigma^2}{\sigma^2 - 0.33} \quad B = 0.45 \frac{\sigma^2}{\sigma^2 - 0.09}$	A diffuse model which considers masking, shadowing, and inter-reflections
3. Lafortune (1997)	$f_r(u, v) = \sum \left( C_{x,i} u_x v_x + C_{y,i} u_y v_y + C_{z,i} u_z v_z \right)^{n_i}$	Uses the notation $u$ for the incident direction and $v$ for the viewing direction, $xy=anisotropy$ , and $y$ is the normal direction.
4. Ashikhmin-Shirley (2000)	$f_{specular} = \frac{\sqrt{(\alpha_x + 1)(\alpha_y v + 1)}}{8\pi} \frac{(h \cdot n)^{\alpha_x \cos^2(\phi_h) \beta_y \cos^2(\phi_h)}}{(h \cdot \omega_o) \max((n \cdot \omega_o)(n \cdot \omega_i))} F(h \cdot \omega_o)$ $f_{diffuse} = \frac{28k_d}{23\pi} (1 - k_s) \left( 1 - \left( 1 - \frac{n \cdot \omega_o}{s} \right)^5 \right) \left( 1 - \left( 1 - \frac{n \cdot \omega_i}{s} \right)^5 \right)$	$\alpha_x$ and $\alpha_y$ control the directions of anisotropy. The leading constant ensures the model meets energy conservation. The Fresnel term $F(h \cdot \omega_o)$ is the Schlick approximation shown below.
5. Schlick Fresnel (1994)	$F(\omega_o \cdot h) = k_s + (1 - k_s) \left( 1 - (h \cdot \omega_o) \right)^5$	A popular choice for the Fresnel term

Stability, such as lights and camera sources, surface variation, and inter-reflections may all have an impact on the quality of the measured data. Additionally, the original representation of the BRDF is problematic to work with. Localized specular reflection, for example, may require a higher sampling rate to increase the specular lobe fidelity (Matusik et al., 2003). An alternate form was proposed by Rusinkiewicz (2011) shown in Figure 6. The half vector parameterization achieves two important goals: *a*) when a material is isotropic it reduces the BRDF to only three-dimensional (3D) parameters,  $\theta_p$ ,  $\theta_h$ , and  $\phi_p$ , and the  $\phi_h$  term may be ignored; and *b*) the half vector also distributes the axes more intuitively along the direction of the specular lobes.

## 2.1 Standardized Gonio-Reflectometers

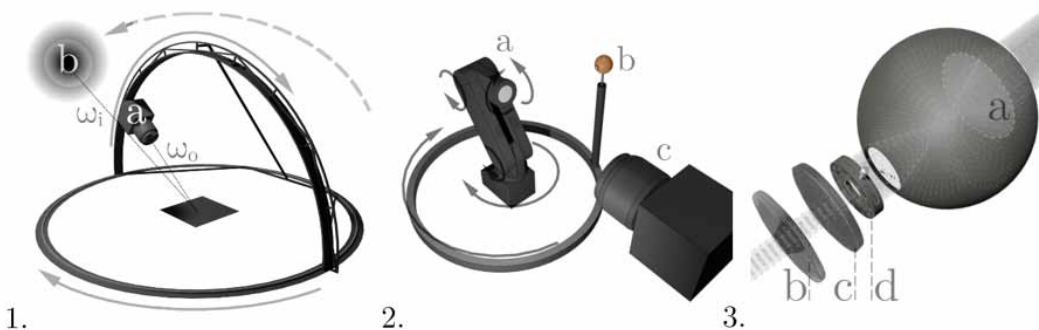
Since Nicodemus' (1977) original formulation of the BRDF, gonio-reflectometers were the first, logical choice for experimentally capturing the reflectance. Gonio-reflectometers usually use a sensor head (such as a spectro-radiometer) on a multi-axis stage that varies the incident and view directions independently. While gonio-reflectometers may represent a "gold" standard of measurement, dense measurement of the surface for computer graphics applications is impractical. Filip, et al. (2013) noted that for a dense sampling of  $1^\circ$  at 1 sample/sec would take many years to complete for a single material ( $90 \times 180 \times 90 \times 180 \approx 2.6 \times 10^8$  samples). Measurements taken on these setups are a sparse sample of the hemisphere, typically in reduced angular steps of  $> 20^\circ$ . Sparse sampling requires interpolation of the missing data to reconstruct a reflectance profile and important features of interaction was lost in the process.

Figure 6. Illustration depicting the change to half-vector parameterization proposed by Rusinkiewicz (2011)



This class of instrument usually represents the most straightforward and logical approach to sampling the BRDF, often consisting of translation stages familiar to the manufacturing industry representing  $n$  degrees of freedom that the device can realize. The field goniometer system (FIGOS) developed by University of Switzerland and Remote sensing laboratories is a typical design of this category of instrument (see Figure 7-1) (Sandmeier & Itten, 1999). The primary end use for the instrument was measuring and interpreting aerial data and making comparisons with satellite applications, such as NASA satellite data. The lightweight, detachable aluminium frame allows the device to be field deployable, and measurements can therefore be taken *in situ*. A spectro-radiometer, mounted to the arc shown in Figure 7-1.a, takes sparsely spaced measurements of  $30^\circ$  steps in the azimuth directions, and the range of  $-75^\circ$  to  $75^\circ$  view of the zenith angle at  $15^\circ$  steps. Hyperspectral measurements from the sensor were of 1.5 to 8.4 nm step resolution of a wavelength range between 300 – 2450 nm (1.5 nm step in the 300–1050 nm bands and 8.4 nm step in the 1050–2450 nm). Taking slices of the electromagnetic spectrum is often of importance in scientific contexts not just for

Figure 7. A typical style of gonio-reflectometer described in Sandmeier and Itten. (1) This particular design is a field portable sensor mount *a*, and the light source *b* is the path of incoming solar irradiance. (2) An illustration of a gonio-reflectometer similar to Baribeau, et al. (2009), showing *a*, the robotic arm and sample holder, *b*, the integrating sphere diffuse light source, and *c*, the spectro-radiometer. (3) The light source configuration referred to in Baribeau, et al. (2009) showing, *a* the light baffle, *b* the collimating optic, *c* the opal glass diffuser, and *d* the controllable aperture.



understanding the true colour of a surface, but also spectral characteristics. Such images are composed of multiple channels and may exist entirely outside of the RGB tristimulus part of the spectrum. The precision of the instrument in the zenith angle is within  $\pm 0.2^\circ$ . It is this sort of reliability and precision that makes these instruments as the benchmark reference for measurement from which the newer, less conventional designs may be compared to.

Anisotropy was measured by calculating the anisotropy factor (ANIF) and anisotropy index (ANIX) to analyze the spectral variability due to anisotropy. In both cases, this is obtained analytically rather than by direct measurement of the anisotropic direction. While this analytical approach fit the purpose of the study, such as in the determination of the normalized vegetative difference index (NVDI) of aerial crop data, direct measurement of the anisotropic direction is preferred in the field of computer graphics. Performing such measurements, preferential in high angular resolution, offers a direct validation of analytical predictions.

The Baribeau, et al. (2009) gonio-reflectometer of the Institute for National Measurement Standards, National Research Council Canada, shown in Figure 7-2, is an example of a precise and calibrated contemporary version of the instrument. A spectro-radiometer senses the sample attached to a 5 degrees of freedom robotic arm with a rotating quartz tungsten light stage of Lambertian distribution. The light source design, illustrated in Figure 7-3, is of particular interest as the housing is a barium sulphate coated integrating sphere opening onto an aperture controlled, opal glass baffle and collimating lens, ensuring unpolarized, uniform distribution at the given angle of incidence. The source is also cooled to a precise temperature. Two spectro-radiometers were used of wavelengths 380-780 nm (1 nm step with 5 nm bandpass), and 380-1068 (4 nm step with 20 nm bandpass). The chosen spectro-radiometers reduce the capture time of the spectral dimension significantly owing to diode array configuration. Measurement of reference standards, rangefinder reflectors, and a bidirectional measurement of pearlescent pigments was demonstrated to a high degree of fidelity.

Li, et al. (2020) constructed a somewhat similar 4 axis gonio-reflectometer design capable of anisotropic measurements using a tungsten broadband light source over the visible spectral range detected by a high resolution spectro-radiometer (1024 samples in the 380-760 nm range of 0.82 to 3.3 step resolution). The spectro-radiometer was coupled to an optical fiber to increase the flexibility of the design. A beam splitting prism was also used in conjunction with the optical fiber to allow for a second detector. The lamp design is similar to that of Baribeau, et al. (2009), which implemented diffusing and collimating optics in front of the beam, and the exit port had an adjustable aperture with a stable source (0.1% variation). Various exposure times were used during capture to account for high dynamic range. The sampling density problem with respect to the anisotropic direction was overcome by limiting the measurement to coarse steps of  $20^\circ$ . The total number of sampling directions reported for the 4 dimension measurement was 5,184. For this study, only  $\frac{1}{4}$  of the hemisphere was sampled for anisotropy, as it was assumed that the material's anisotropic direction was symmetric.

## 2.2 Hybrid Devices

A slight departure from the expected gonio-reflectometer design often replaces the sensor head (typically, some sort of spectro-radiometer) with a CCD array, and varying degrees of modification to either speed up the measurement time or accommodate additional features, such as 3D scanning. Lyngby, et al. (2019) described a gonio-reflectometer instrument in which an arc of light sources spaced at  $7.5^\circ$  intervals encompasses the measured object over a  $90^\circ$  arc capable of measuring isotropic materials. A robotic arm of six degrees of freedom, on which the RGB, 9 MPixel CCD sensor is located, is used in conjunction with the arc to measure the complete isotropic BRDF at a reduced sample resolution taking into consideration the symmetry of Helmholtz reciprocity. Radiance was measured by taking a comparison measurement from a Spectralon standard. A dark spot at the illumination location existed, due to the convergence of the camera and source at the location, and some reconstruction errors were observed for the specular highlight, due to the limited sample density of the highlight.

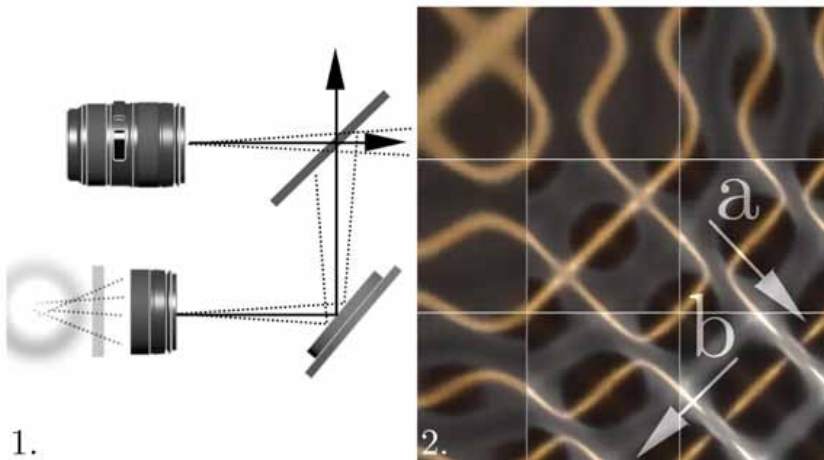
Several papers were published based on measurements made on a device known as the Stanford spherical gantry shown in Figure 8-1. Some examples are the BSSRDF described by Jensen, et al. (2001), and light scatter modeling of human hair described in Marschner, et al (2003). The gantry consisted of two rotating arms, one housing the point light source or light projector, and the other housing the imaging device, enabling various degrees of freedom dependent on the configuration.

Holroyd, et al. (2010) use the design of the Stanford measurement gantry to mount a stereo pair of “coaxial” camera and light sources separated by a beam splitter, illustrated in Figure 9-1. The light source is a tungsten halogen source with mechanical shutter. This arrangement allows both the measurement of the BRDF and the geometry of a 3D object. A high-frequency, spatially-modulated, sinusoidal light source is introduced as a structured light capability to achieve this end. Unlike many projector variants, the modulated light is achieved using a mechanically operated optic, thereby, avoiding some inherent issues with digital projection, such as the screen door effect.<sup>1</sup> Geometry is

Figure 8. (1) The Stanford gantry consisting of *a* the camera mount, *b* a movable light source/light projector, and *c* the sample stage. (2) The UTIA gonioreflectometer described by Filip et al. With camera *a* and light source *b* (3) Diagram of the PAB Goniophotometer II described in Dupuy and Jakob, where *c* is the sample holder and *b* is a fixed light source relative to the movable axes Note that the camera may be replaced by a spectrometer sensor head in some cases.



Figure 9. (1) The arrangement of the camera and light source described by Holroyd, et al. (2010). (2) The cumulative adaptive slice measurements described by Filip et al. showing the specular direction *a*. and the anisotropic direction *b* (Filip & Vávra, 2014).



claimed to be accurate to within 50  $\mu\text{m}$  of the true surface geometry, even on challenging surfaces, which are highly reflective. A tuneable *Varispec* LCD filter was introduced into the camera's optical path to generate accurate RGB filtered exposures on the monochrome sensor. The system has the potential to capture multi-spectral images, as other researchers have done (Baribeau et al., 2009) (Dupuy & Jakob, 2018). The stereo image capture capability as described by Holroyd, referred to as the reciprocal image pair, has several benefits, such as simultaneous calibration of camera and light sources, mitigation of unwanted specular effects from a single camera view, and occlusions given that two viewpoints are observed.

Photometric stereo reconstruction is avoided in favor of an "active multi-view stereo" algorithm developed by the researchers to stitch together the scans from multiple views. This avoids estimation error in cases when an object's reflectance deviates from an ideal diffuse model and the estimation is difficult. The setup is limited with regards to low albedo objects or perfect, mirror-like reflectance.

BRDFs may also consider interfaces other than that of air and the material surface. Marschner, et al. (2005) examined the interface of various woods coated in varnish. The BRDF was measured using the Stanford spherical gantry. Wood is observed to have a layered air-cellulose interface and light is reflected from the interface in a cone perpendicular to the fiber direction, and due to the irregularity of the fiber layers, the scattering is distributed about the cone. The surface layer of unfinished wood is somewhat diffuse due to the manufactured surface finish that damages the cells. When the varnish is applied, because the finish is approximately the same index of refraction as the wood, the more diffuse surface is eliminated, causing the subsurface to become more prominent. A specular highlight was observed for the subsurface, which was different from the reflection and spatially variable over the surface.

### 2.3 Enhanced Parameterized Measurement

The parameterized approach attempts to overcome the limitation of long acquisition times of gonioreflectometer devices. Instead of measuring the entire BRDF for all the dimensions, the most salient parts of the measurement are first determined. This has an advantage when the anisotropic dimension is measured, as the extra dimension prohibitively increases the acquisition time and data storage requirement. Filip, et al. (Filip & Vávra, 2014; 2013) attempted to solve the sparse sampling problem inherent to most designs by creating an adaptive algorithm which populates the most salient parts. The instrument shown in Figure 8-2, takes 6,561 samples from a CCD sensor of  $81 \times 81$  directions, or alternately a slightly denser set of 22,801 samples from  $151 \times 151$  directions, taking approximately 18 hours to complete. Low dynamic range images for each direction of different exposures are combined to form a high dynamic range image. Samples are illuminated from LEDs representing the incident direction. The sparsely populated samples points are taken in a helical pattern over the hemisphere. These points are used to construct slices of the anisotropic BRDF, unlike commonly used interpolation techniques, shown in Figure 9-2, interpolated from  $2^\circ$  down to  $0.5^\circ$ . A slice can, therefore, be thought of as a 1D signal. These slices are arranged to form diagonals consisting of an axial slice representing the direction of specularity of the material and characterizing its anisotropic properties, shown in Figure 9-2.b. A perpendicular slice forms the diagonal slice which captures the shape of the specular peak, shown in Figure 9-2.a. The authors claim that a highly accurate reconstruction can be obtained using 12 of these slices,  $30^\circ$  apart in the azimuth direction. For the technique to work correctly, the anisotropic direction must be determined *a priori*. True specular materials are limited in the resulting dataset, as there is insufficient samples for proper sampling. The researchers highlighted a lack of available densely populated anisotropic data in the literature, citing the lack of such publicly available anisotropic data in validating their technique. The ground truth is obtained from a ray traced analytical model (Kurt (2010)), and validated with sparse gonioreflectometer measurements. A later paper on the technique argues the data has less reconstruction error compared to non-adaptive reconstruction (Filip & Vávra, 2014).

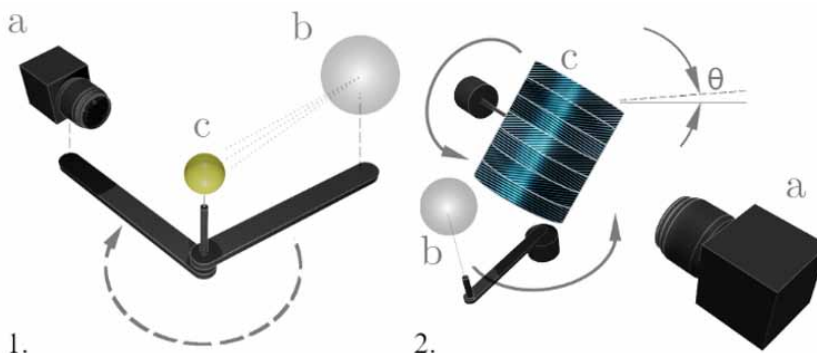
Dupuy and Jakob (2018) adopt a similar adaptive parameterization approach to sparsely sampled data. Measurements were taken on a commercial instrument, the *PAB Gonio-photometer II*, shown in Figure 8-3. The Gonio-photometer uses a fixed xenon arc light source and a spectrometer of approx. 3.3nm spectral resolution of wavelength range 360-1000nm. Exposure times are manually determined based on the specular highlight. Data acquisition for isotropic samples is 3,712 samples, and for anisotropic sample this is increased to 118,784. The acquisition rate occurs at approximately 0.5-1Hz, this equates to approximately 2.5 hours for isotropic samples, and 2-3 days for anisotropic materials.

The adaptive parameterization approach, described by Dupuy and Jakob, introduces a new spectral BRDF material database of 36 different materials, with 4 of the materials having an anisotropic direction. The researchers compute a micro-facet distribution from retro-reflective measurements and then use the distribution to define an important sampling direction. These salient parts are used to focus the measurement where it is most needed and thereby reduce the overall capture time considerably. A point that is often overlooked in adaptive techniques, which was duly noted by Dupuy and Jacob, are the basic sampling theorem requirements for reconstructing a signal determined by the original signal's frequency. The technique showed less efficiency however with multi-lobe materials, *i.e.* materials that have layered or composite characteristics such as plastics, and translucent materials are also problematic. One interesting advantage of the method is that the data can be stored compactly without further optimization.

## 2.4 Image-Based Techniques

All of the previous mentioned designs share the common problem of sparse data sampling due to the amount of time taken to measure each sample, although the more recent designs described overcome this problem somewhat. Unconventional designs of various forms, which use a camera CCD as a 2D sensor area, are attempts to reduce the required degrees of freedom, or problems introduced with mechanical movement by eliminating the number of moving parts required. Out of these investigations, the Mitsubishi Electric Research Laboratory (MERL) 100 database has had significant influence on the field of computer-generated imagery and is one of the most cited comprehensive published databases. Based on the work of Marschner, et al. (2000), the problem of viewing direction is transformed into a sample space which is spherical. The sample sphere allows the simultaneous measurement of multiple viewing directions in high resolution by tracing the path between the pixel and the surface normal on the sphere (see Figure 10-1). Each pixel, therefore, represents an angular measurement placed into bins  $\theta_p$ ,  $\theta_r$ , and  $\phi_d$ . Measurements from a 1.3 Mpixel imaging device were densely sampled over the hemisphere, taken from spherical-shaped samples consisting of the homogeneous material under

Figure 10. (1) Illustration of the measurement of the MERL 100 showing *a*, the viewing direction, *b* the light source, and *c* the sample sphere. (2) The measurement cylinder described by Lu, et al. (2000) and Ngan, et al. (2005) where  $\theta$  is the angle of anisotropy for each strip, *b* is the incident angle and *c* is a motorized stand.



investigation. High dynamic range photographs consisting of 18 low dynamic images were taken for a total of 330 high dynamic range (HDR) images over the hemisphere. The advantage of the technique, which takes 3 hours per sample, is that the image plane essentially acts as numerous 1D sensors. The half angle vector coordinate system was used to densely sample the specular highlight which requires higher sampling for reconstruction fidelity. As the materials under investigation were isotropic, a 3D BRDF data set was acquired consisting of  $90 \times 90 \times 180$  bins for each RGB channel. The dimensions were reduced by half because the measurement observed Helmholtz ( $\theta_d, \theta_h$ ) and bilateral symmetry ( $\phi_d$ ). Perhaps of greatest significance, is the use of the data set in fitting analytical models or comparing and validating new techniques (Matusik et al., 2003).

Lu et al. (2000) noted in their study of anisotropic materials however, that a spherical sample space was more suited only to liquid coatings, such as paints, as certain types of materials cannot be easily conformed to the shape of a spherical ball. Anisotropic measurement is not feasible using this method. Dupuy and Jakob also noted that it was difficult to determine in some cases which parts of the MERL data were “real” or interpolated. Burley also observed data beyond  $75^\circ$  appears to be extrapolated, and anomalies with fabrics near grazing angles were suggestive of stretching and wrinkling (Burley, 2012). Lu et al. (2000) instead proposed an acquisition method for measuring anisotropic materials, such as velvet, consisting of a cylinder wrapped with numerous sample of strips, a rotating light source, and a stationary camera relative to the cylinder, shown in Figure 10-2. The study was composed of six strips  $30^\circ$  apart in the anisotropic direction. Whereas, Ngan et al. (2005) expanded on the direction of anisotropy of each strip in a similar study which varied at  $9^\circ$  intervals over the cylinder covering a  $180^\circ$  hemisphere. The cylinder was also rotated over a  $180^\circ$  hemisphere lengthwise. Ngan provided further analysis of measured BRDFs against physically based models which subsequently set the stage for future analysis and data fitting techniques. The combination of rotation and orientation of the samples provide an anisotropic set of  $45 \times 45 \times 180 \times 180$  bins for each of the three RGB channels. It was found that for some anisotropic materials the micro geometry of the surface causes a complex interaction that was not easily modeled by analytical models.

A more recent approach to this technique considers the polarization dimension in the measurement. Baek et al. (2020) created the first dataset of wavelength dependent polarized BRDFs (pBRDF) using an image-based acquisition setup. A FLIR machine vision camera was used to image spherical sample materials illuminated by a broadband LED source, using a similar technique to the previously mentioned in Marschner et al. (2000) and Matusik et al. (2003) studies. Multi-spectral filters with a bandwidth region of 10 nm were used to capture wavelengths of 450, 500, 550, 600, and 650 nm. Both linear and circular polarization were measured, and the chirality of the polarization was recorded. Approximately 6-8 exposures were taken of each sample measurement and combined to form a HDR image, and the device was radiometrically calibrated with a spherical Spectralon sample for each wavelength. Each sample consisted of 26,460 HDR images, representing 147 lighting directions, 5 spectral bands, and 36 unique polarized states, and took 2.5 days to complete. Inverse mapping was used to correlate pixels in the image with angular data. Different isotropic materials were recorded in the dataset with a storage size of 912MiB per material for the 25 materials recorded. Each material consisted of bins  $\theta_d$  (91),  $\theta_h$  (91),  $\phi_d$  (361), and  $\lambda$  (5). The  $\phi_d$  was extended compared to previous studies as it was noted that the bilateral symmetry assumption ( $\phi_d = 180^\circ$ ) does not hold for pBRDFs.

While human perception is unable to discern polarization acting on a material, the Baek et al. (2020) study argued a relationship exists between the polarized state of the reflectance and the specular profile. They demonstrated a direct dependency through examination of the polarized state between surface normals and diffuse reflectance, linking diffuse polarization and the material’s surface roughness. The link may have importance for inversely determining material rendering based on the measurement using a data driven approach. The researchers also demonstrated, experimentally, the wavelength dependence of polarization.

Yang et al. (2020) take a mirror approach using a semi-circular ring as the reflecting element. This has the advantage that the BRDF can be quickly and easily discerned using basic imaging

optics directed toward the front face of the ring, as shown in Figure 11-1. For the measurement, a sample of the material is placed at the center of the ring. The reflecting rays from the light source positioned behind the ring at the incident angle  $\omega_i$  are directed toward the image sensor based on the ring's geometry. The occlude,  $c$  in Figure 11-1, prevents any stray light incident on the surface from interfering with the image.

## 2.5 The Bidirectional Texture Function

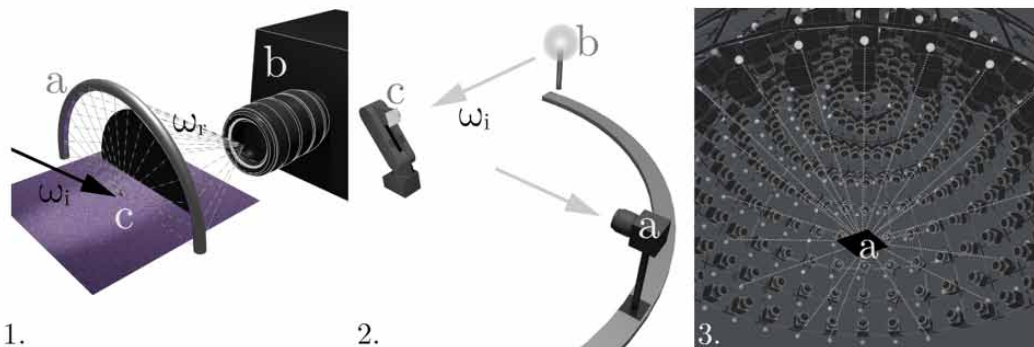
As noted by Schwartz et al. (2014), the BRDF is limited in its power to describe certain materials adequately, such as when the surface is non-uniform. This is especially the case for textiles, which have some variation over the surface due to the fabric weave, although any non-uniform surface is potentially problematic. Variation may be the result of occlusion, inter-reflections, and other geometry-specific phenomenon, as is the case for micro-faceted geometry, and also subsurface scattering may play a role. At the very least the arrangement of fibers are likely to cause non-trivial anisotropic effects, which need to be accounted for in the measurement.

The BTF, as described by Dana et al. (1999), is the textured appearance of the surface dependent on the viewing and lighting directions. The BTF may be described as a 6D non-local reflectance field,  $L(x, y, \theta_o, \phi_o)$ , for capturing a planar geometry and accounts for such effects due to the non-localized imaging of the surface. It is often convenient to think of the data as a stack of 2D textures  $xyz$ , each representing an angular viewing  $\omega_r$  and lighting direction  $\omega_l$ .

$$b(x, y, \omega_i, \omega_o) \tag{9}$$

The BTF is similar in principle to the 6D SVBRDF except the reference geometry is assumed to be planar instead of a complex 3D shape. Schröder et al. (2012) go further, and consider the BTF and BRDF to be “simplified” methods, and describe many volumetric approaches which encompass the indeterminate “fuzzy” boundary layer, such as fibers above the surface of a textile (e.g. mohair). These volumetric rendering techniques are essentially statistical models of the boundary layer volume. Some examples are the micro-flake model, a model similar in principle to the micro-facet model except applied to a volume area, and the Gaussian Mixture Model, a statistical model of fiber densities and distribution. Schröder, et al. draw similarities in volumetric approaches between hair studies and that of textiles (Schröder et al., 2012).

Figure 11. (1) The basic design of the semi-circular ring as described by Yang et al. (2020) where  $a$  is the image sensor device location,  $b$  is the semi-circular ring, and  $c$  is the occlude. (2) An illustration of the first BTF measuring device at the Uni. of Bonn, Germany, a gonio-reflectometer design showing the position of  $a$  the camera,  $b$  the light source, and  $c$  the robot arm and sample. (3) Illustration based on the second device at the Uni. of Bonn, showing the inside of the dome camera array, where  $a$  is the location of the sample.



The rendering is time for most volumetric techniques, however is impractical for real time applications and mostly limited to offline ray traced rendering. A review was conducted by Wu and Yuksel (2017), and the conclusion drawn by the authors is that even though realism is significant, they are “highly expensive in storage and computation.” Some limitations of BTF measurement discussed by Schröder, et al. included light diffusion, silhouetting, and transparency. These discrepancies may be a matter of application rather than a true limitation of technique. Schwartz, et al. also claims that the BTF cannot measure subsurface scattering, or translucent and transparent materials, yet there is no identifiable reason stated why this is infeasible.

Some of the previously mentioned instruments can be capable of BTF measurement. The capture of BTF measurements, however, has expanded to a whole class of instruments built specially for this purpose. Usually, these encompass some sort of camera CCD array given that cameras are the most practical option for recording a planar array of measurements per angle. Schwartz et al. (2014) built three such devices, one gonio-reflectometer type of instrument, and two dome-like camera arrays. The latter instrument was an attempt to improve the acquisition based on certain shortcomings as discussed in the research.

Some of these improvements of the latter devices included the amount of CCD sensors, which is reduced to a cluster of 11 about an arc of  $90^\circ$  over the hemisphere. The previous version attempted to cover the entire hemisphere in inexpensive point-and-shoot cameras, and the flashes on these cameras also inadvertently introduced fluctuation errors. The number of light sources (198) is increased to cover the hemisphere, speed up the measurement time, and achieve greater directions of  $198 \times 264$  of  $7.5^\circ$  and  $15^\circ$  steps, respectively. The intensity of the LEDs is the limiting factor in the design, which require longer exposures depending on the material, although the authors claimed a phosphor coating overcomes the spectral limitations of solid state lighting. The capture time is therefore 4-10 hours and an additional 1.3-3 hours reconstructing the 3D geometry. Image ranges are, BTF:  $11 \times 3 \times 198 \times 24 = 156,816$ , and structured light:  $11 \times 3 \times 42 \times 8 \times 4 = 44,352$ . The data size for the images is significant at 918.8 Gb and 259.9 Gb, respectively.

In summary, the gonio-reflectometers can achieve high accuracy measurements, and are more intuitive machine stages in their construction, yet often suffer from lower resolution and the possibility of technical vibration from moving parts. Image-based devices generally offer higher resolution, and less moving parts, but the sample space is abstracted from the aforementioned machine-like stages of the goniometer devices, and the malleability of the sample over the geometry may be a limitation. BTF devices are a significant improvement, where the material’s appearance is non-uniform, especially with regards to textiles. Yet, the required amount of data is significant, and it is not uncommon to find devices that require long acquisitions or complex, expensive designs.

### 3. DATA FITTING

BRDF and BTF measurements may not be suitable for use with computer renderers directly because it is inefficient to render the raw data directly requiring significant graphics processing unit (GPU) resources. The data also cannot be easily edited, changing parameters such as the perceived roughness, or colour of the material. Therefore, data fitting is done in order to create a realistic approximation that is compactly represented in hardware that closely matches the measured material.

This section outlines the methodology of transforming captured reflectance data into a form that can be displayed in a computer simulation. The first part outlines important studies of measured datasets which were used to fit the parameters of analytical models into a physically based rendering pipeline. The importance of the Cook-Torrance, micro-faceted model is contextualized with regards to the choice of the  $D$ ,  $G$ , and  $F$  terms used in a commercial context for real time rendering applications and efficient animation rendering. They describe how materials are evaluated, from the choice of the analytic model to the so-called “artistic” parameters one uses to alter the appearance of the material. Contemporary approaches to how data fitting is

being performed in the literature are also reviewed, and several examples are discussed of data driven, and hybrid methods. The data driven method implies an inverted technique which starts with measured data and works backward to find a model, whereas hybrid models attempt to leverage aspects of both techniques to solve the fitting problem.

### 3.1 Parametric, Physically-Based Modeling

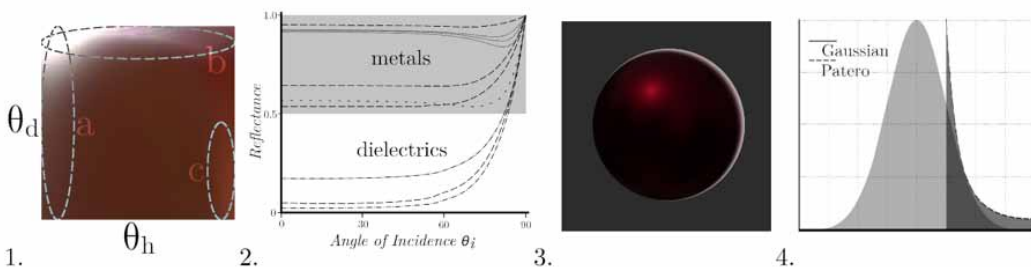
Data fitting to existing or slightly modified analytical models is desirable because analytical models offer compact representation, may be easily modified through “artistic” parameters, and are well established in commercial rendering platforms. Numerous analytical models have been reported. The introduction in the literature of measured, high resolution, BRDF databases has been invaluable for providing a reference to determine the best fit for each of the terms. Ngan et al. (2005) compared analytical models against a measured dataset, the Matusik et al. (2003) MERL 100. Burley (2012) found that the dataset, however, was most influential commercially in physically-based rendering pipelines, and has led to its widespread adoption with minor modifications by leading industries. The Burley’s study is commonly referred to as the “Disney” or alternately, the “principled” model, the latter is with regards to *ad hoc* choice of principles that are more accessible to artists.

One of Burley’s key contributions was a novel way of looking at the MERL dataset for visual clues as to each component of reflectance that should be present in the analytical model. Slices of images of dimensions  $\theta_d$  and  $\theta_h$ , which form a stack of 180 images reveal the unique properties of each material. When the condition  $\phi_d = \pi/2$  is satisfied the most salient features are observable, shown in Figure 12-1. Different areas of the image correspond to the diffuse component, the specular and Fresnel peak, and the retro-reflection of the material.

The datasets reveal that true Lambertian diffusion is rarely observed in practice and even subsurface models failed to predict a retro-reflective peak seen at grazing angles on some materials. With regards to the roughness  $D$  term, of Equation 10, Ngan et al. (2005) found, experimentally, that for each case, Beckamn, Gaussian, and cosine power, the fitting quality was “nearly identical both numerically and visually.” Experimental results confirmed previously known inaccuracies of Phong and Lafortune, with respect to the clipping of the angle of the half vector.

In the Burley (2012) model which is commonly used by commercial renderers, the GGX/Trowbridge-Reitz model is chosen for the  $D$  term, where  $\alpha$  is the roughness parameter, shown in Equation 10 (Karis, 2013). It was observed that while this model requires slightly more GPU resources to render than the previously used term of Cook-Torrance model, BRDF measurements demonstrate longer specular tails, deviating from Gaussian distribution. Thus, the benefit was the increased realism of the model in capturing this characteristic trait.

Figure 12. (1) A slice of the tabulated data similar to Burley where  $\theta_d = \pi/2$ : a. is the specular peak, b. is the Fresnel peak, c. is the grazing retro-reflection (Burley, 2012). (2) Fresnel reflectance for metals and dielectrics. (3) Illustration demonstrating the prominence of the Fresnel component near the grazing angle. (4) Gaussian distribution vs power law / Paterno distribution.



$$D(h) = \frac{\alpha^2}{\pi((n \cdot h)(\alpha^2 - 1) + 1)^2} \quad (10)$$

The shadowing  $G$  term is commonly based on the Schlick (1994) model, shown in Equation 11, where,  $k$  term is said to reduce the gain for shiny materials, and  $k = (\text{roughness} + 1)^2 / 8$ . The  $G$  term does not hold for image-based lighting, which produces attenuation at glancing angles that is too dark. Burley (2012) noted the term has significant impact on the albedo of the material, causing a gain at grazing angles. The measured data gain is due to non-specular phenomenon and also may be the result of grazing retro-reflection, especially with regard to rough materials.

$$G_1(v) = \frac{n \cdot v}{(n \cdot v)(1 - k) + k} \quad G(l, v, h) = G_1(l)G_1(v) \quad (11)$$

The Fresnel-Schlick approximation, model 5 in Table 1, is currently a popular choice for  $F$  despite the complexity of calculating the Fresnel coefficients. A further approximation is made with regards to the index of refraction, due to the fact that the Fresnel-Schlick approximation is undefined for conductors. The term  $F_o$  is a per-measured value approximation taken from the perpendicular, normal incidence angle. It is usually an RGB vector term, given that conductors are often tinted. This is often referred to as the specular color of the material. While it is technically possible to alter the specular color of dielectrics for artistic reasons, specular color is most usually associated with metals in physically based materials.

The energy conservation model accurately describes both the reflectance (specular component) and refraction (diffuse component) as the light hits the surface. BRDF rendering further assumes that the subsurface scattering distance is localized to a small lateral area and ignores the rays that exit at a greater distance. Therefore, the conservation model is the integrated components of the reflection and refraction that does not exceed 1.0. The “white furnace test,” described by Heitz (2014) and shown in Equation 12 ensures the conservation of energy is maintained for micro-facet shadowing and that materials do not absorb or radiate too much energy. Lack of energy conservation will be seen as materials that are either too dark, or too bright. This is primarily due to incorrect modeling of scattering which does not take into account multiple scattering events.

$$\int_{\Omega} f_x(\omega_o, \omega_i) | \omega_i \cdot n \cdot d\omega_i = 1 \quad (12)$$

It is assumed that the light is entirely occluded by the shadowing function  $G$ , whereas inter-reflections do contribute some indirect scattered component to the overall output of real materials. The micro-faceted model absorbs more light than it should in reality, and in this sense fails the furnace test, appearing too dark. The models fail the energy conservation because the shadowing term  $G$  is the most complex interaction to describe accurately in any analytical BRDF (Ashikhmin et al., 2000). This is because there are many possible micro-geometries that satisfy the shadowing present in the micro-facet distribution.

Another potential failure mechanism is with respect to the reflection direction. The incoming and viewing angles of the BRDF are subject to Helmholtz reciprocity, such that the angles are reversible with respect to any absorption, refraction, or reflection that may have taken place. Often, theoretical BRDFs violate this principle. The Cook-Torrance BRDF is a good example of reciprocity failure. Due to the difficulties of modeling the Fresnel term directly, inaccuracies may be introduced. The Schlick approximation, for example, has trouble modeling the reflectance accurately for metals as the

angle of incidence approaches grazing angles, this is due to a characteristic dip before the start of the exponential increase towards grazing, which is not accounted for by approximation, see Figure 12-2.

For some materials localized reflectance is insufficient to describe the material properties and a more computationally expensive subsurface scattering model may be employed separately to describe certain surfaces, such as skin or wax. To fit the data numerically to these analytic functions, a cost-based function is used, usually a squared error loss  $L_2$  metric. The numeric fit quantifies the amount of error between measured, tabulated data and the analytical model. Some methods discussed in the literature are the cosine weighted square distance (Ngan et al., 2005; Whitted, 1980), a log-based function (Sun et al., 2018), and a cubic root function, shown in Table 2 (Forés et al., 2012) (Lavoué et al., 2021).

It is generally accepted that due to the non-linearity of BRDF materials, the log and cubic root models perform better; however, no cost function performs accurately on all materials (Forés et al., 2012) (Sun et al., 2018) (Bieron & Peers, 2020). A common issue with the cosine weighted square distance, for example, is the strength of the specular component, which tends to dominate the square error, over emphasizing the highlight. Log-based fitting is one potential strategy to mitigate such an

**Table 2. Cost functions used to fit measured datasets to analytical models, where  $f_r$  is the measured, tabulated BRDF data,  $f_a$  is the analytical model and  $N$  are the tabulated components, e.g. for an isotropic BRDF  $N=\theta d \times \theta h \times \phi d. \times 3$  channels (RGB)**

#	Method	Function	Comments
1	Root Means Squared	$E(p) = \sqrt{\frac{\sum (f_r(\omega_i, \omega_o) - f_a(\omega_i, \omega_o, p))^2}{N}}$	A simple root means square error metric fitting function.
2	Cosine Weighted	$E(p) = \sqrt{\frac{\sum (f_r(\omega_i, \omega_o) \cos \theta_i - f_a(\omega_i, \omega_o, p) \cos \theta_i)^2}{N}}$	Cosine angle compensates for an increase of reflectance at grazing angles
3	Cubic Root	$E(p) = \sqrt[3]{\frac{\sum ((f_r(\omega_i, \omega_o) \cos \theta_i - f_a(\omega_i, \omega_o, p) \cos \theta_i)^2)^{1/3}}{N}}$	Reduce the influence of the peak which otherwise dominates the fit
4	Log1 and log2 (Sun et al., 2018)	$E(p) = \frac{\sum \left  \log \left( \frac{f_r(\omega_i, \omega_o) c(\theta_i, \theta_o) + 10^{-3}}{f_a(\omega_i, \omega_o) c(\theta_i, \theta_o) + 10^{-3}} \right) \right }{N}$ $E(p) = \sqrt{\frac{\sum \left( \log \left( \frac{f_r(\omega_i, \omega_o) c(\theta_i, \theta_o) + 10^{-3}}{f_a(\omega_i, \omega_o) c(\theta_i, \theta_o) + 10^{-3}} \right) \right)^2}{N}}$	The cosine map evaluates as: $c(\theta_i, \theta_o) = \max(\cos(\theta_i), \cos(\theta_o), 10^{-3})$
5	Bieron and Peers (2020)	$E(p) = \sum \left  \Lambda(f_a(\omega_i, \omega_o; p) \cos \theta_i \gamma) - \Lambda(f_r(\omega_i, \omega_o; p) \cos \theta_i \gamma) \right ^2$	Where: $\Lambda$ is a compression function, and $\gamma$ controls the amount of compression.
6	SSIM	$SSIM(x, y) = \frac{(2\mu_x \mu_y + c_1)(2\sigma_{xy} + c_2)}{(\mu_x^2 + \mu_y^2 + c_1)(\sigma_x^2 + \sigma_y^2 + c_2)}$	Where: $\mu$ = the average, $\sigma^2$ = the variance, $\sigma_{xy}$ = the covariance, and $c_1, c_2$ are stabilizing variables consisting of a saturation coefficient and the dynamic range $L$ ( $c_1 = (k_1 L, c_2 = (k_2 L)$

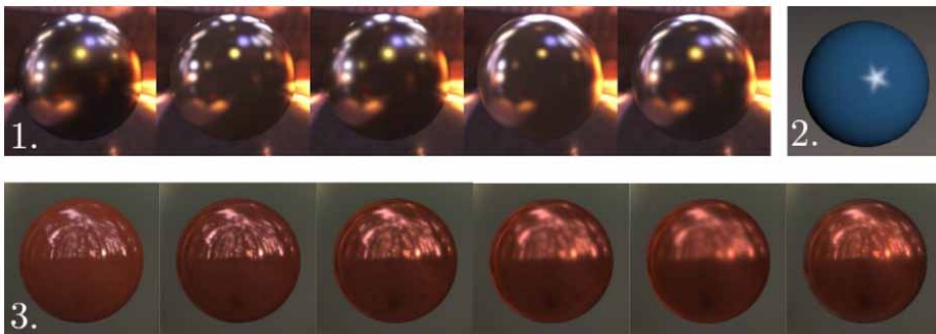
effect by compressing the dynamic range non-linearly so that specularity does not skew the weighting. Log-based fits however tend to blur the highlights of the material. Lavoué et al. (2021) reported that a feasible strategy is to first reduce the influence of the peak by taking the cubic root of the BRDF prior to computing the  $L_p$  distance, and resulted in superior fits.

Of important note is that regardless of the metric used, measured data does not follow the usual parametric Gaussian and Phong distribution used in analytical models, and instead exhibits sharp, scattering curve peaks with an inverse-power-law distribution. Therefore, much of the literature takes Gaussian distribution as an assumption of the model and introduces a specular rendering error predominantly at the tail of the distribution. (Löw et al., 2012) It was observed that multilayered materials, such as metallic paints and brushed metals, were poorly modeled by single lobes of reflectance; however, an extra lobe reduces the fitting error by as much as 25%. (Ngan et al., 2005) Another limitation is the reliance of many studies on evaluating the MERL 100 dataset, which contains no anisotropic materials.

For the anisotropic case, Ngan et al. (2005) began with an earlier version of the BRDF model reported by Ashikhmin et al. (2000), and rearranged the micro-facet term to the left hand side. This allowed for the input of measured data to solve for the micro-faceted term by observing that the BRDF is proportional to the micro-facet distribution, when ignoring shadowing and masking effects. Shadowing, masking, and the Fresnel term of the distribution were obtained through an iterative trial and error process. An advantage of this model is that it may accommodate unusual distributions as illustrated in Figure 13-2.

Numeric metrics alone are insufficient instruments to evaluate the fit and use both numerical and perceptual or imaged-based metrics. Forés et al. (2012) began with different numerical metrics and fitted one diffuse analytical lobe and two specular lobes to the 10 materials from the MERL 100. They then conducted a user perceptual observer study to determine the best fit using the two-alternative forced-choice (2AFC) approach. The reference image was rendered from the tabulated data and the observer asked to choose the closest match between alternative choices. Bieron and Peers (2020) initially took the common route of fitting numerical cost functions, but added an important image processing step that determines perceptual-based similarity without an observer trial. It could be argued this is the logical next step in data fitting evaluation. The paper correctly identified that although visual appearance is significant, cost functions are evaluating a numeric quantity, which does not account for visual perception. Furthermore, simple image similarity metrics, such as the mean square root error (MSRE) and the *peak* signal to noise ratio (PSNR), fail to quantify perceptual differences. This is because they are independent pixel-wise evaluations of absolute error, yet two

Figure 13. (1) Ngan et al. (2005) (from left to right) measured result, Cook-Torrance (single lobe), Cook-Torrance (2 lobe), Lafortune (1 lobe), Lafortune (2 lobes). (2) Perhaps one reason why the Ashikhmin et al. (2000) method was chosen to represent the anisotropic data was in its presented ability to represent unusual, or even physically impossible micro-facet distributions. (3) Bieron and Peers (2020) showing values of  $\gamma$  from left with reference BRDF on right ( $\gamma=1.1, 1.5, 1.9, 2.3, 2.7$ ).



images may retain similarities even though they may be dissimilar at the pixel level. Therefore, the approach is a twofold operation whereby data is first fitted by cost function evaluation, and then a perceptual-based image metric judges which metrics are most faithful. The two metrics used were a color-based structural similarity index metric (CSSIM) and the learned perceptual image patch metric. The CSSIM algorithm uses statistics such as the average, variance and covariance based on a weighting of the luminance, contrast, and structure of the image. The structural similarity of method 6 in Table 2 is the measured difference between two image windows  $x$  and  $y$  of dimensions  $n \times n$ .

The measurement may be valid from -1 to +1 (where -1 is considered perfectly dissimilar) but is usually taken in the range of 0 to 1. There is no basis for considering a temporal domain for the original formulation, but animations may be compared by examining pairs of frames in a sequence. Other temporal versions exist for video sequences. This may be of some importance in evaluation of BRDFs where a single image of the surface is not sufficient to describe fit.

The fitting metric of method 5 shown in Table 2 is a slightly modified cosine weighted function where the parameter  $\lambda$  is a compression function  $\lambda(r; \gamma) = r^{\lambda/\gamma}$ , and  $\gamma$  controls the amount of compression. When  $\gamma = 1$ , the function resembles the classic cosine weighted function. Higher values of  $\gamma$  tend towards a diffuse surface with blurry highlights, and lower values emphasize the specular highlights, shown in Figure 13-3.

Lavoué et al. (2021) used numerical analysis, a perceptual study and an image-based metric to evaluate 9 analytical models against tabulated data from the MERL 100. The perceptual study was similar to the Forés et al. (2012) where an observer rates the closest fit of image pairs. Numerous numerical and image metrics were used, including the structural similarity metric used by Bieron and Peers (2020). It was found that using rendered spheres to assess reflectance is the least optimal approach and recommend geometry with both concave and convex curvature. Lavoué et al. (2021) noted that the Log 2 metric of method 4 in Table 2 performed the best correlation with observer impressions.

### 3.2 Data-Driven Fitting

The goal of non-parametric fitting begins with a measured dataset and performing an efficient compression algorithm. Just as image-based compression is dependent on the frequency of the image, it may be plausibly argued that materials also have finite compression due to high frequency optical characteristics. However, non-parametric models can represent a wider gamut of materials at the expense of efficiency in some cases. Generally speaking, the compression seeks to find features of importance, which are retained or use some interpolation methods. Singular value decomposition and principle component analysis reducing algorithms have been used repeatedly for BRDF compression (see for example, Dana et al. (1999), Matusik et al. (2003), and Weinmann et al. (2014)). These techniques take the measured angular data into matrix form and attempt to find the best fit by classifying (extracting) the specular reflectance in the eigen space. Another common property that non-parametric modeling may exploit is separability of reflectance into a linear combination of diffuse and specular components. The separability may also be exploitable for artistic parameters, which can change the appearance of these features.

Lawrence et al. (2006) (Weyrich et al., 2009) (Cook, 1984) describe that inverse shading trees is a good example of the non-parametric technique, which essentially factors measured BRDFs into a small number of low dimensional components using singular value decomposition. It is loosely based on the work of Cook (1984) who attempted to apply a shading tree structure of basis components that make up a theoretical BRDF. The inverse tree implies that the operation proceeds from a known material and attempts to infer the basis components of the non-parametric theoretical model that best fits the surface profile. Basis decomposition may be increasingly relevant to non-parametric representation techniques, and it is argued that real world surfaces are only composed of a “component” or “basis” materials distributed on complex spatial patterns. Another good example is an object which may be manufactured using only several distinct materials, each of which adds a contribution to the overall reflectance profile. Inverse shading trees decompose the surface into a tree structured hierarchy, a

collection of lower-based functions that correspond to the intuitive features of the sample. The top-level decomposition, for example, would be the sum product of a set of 4D functions (basis BRDFs) and 2D weight maps that describe spatial blending, referred to as the coordinates in the basis. Further decomposition is performed, forming the tree, whereby 4D basis BRDFs are decomposed into 2D (maps) then 1D (curves which describe the reflectance profile). Each leaf of the tree captures elements, such as the shape and size of the lobe and the spatial distribution over the surface of each component. The authors argued that the goal to making intuitive edits of the angular and spatial components lies in choosing the correct sum of component BRDFs and their spatial distributions. Editing the angular component, for example, may be used to alter the roughness or the anisotropy. Editing the spatial component remaps the reflectance on the material. The key contribution by Lawrence, et al. was an algorithm whose constraints are non-negative, energy conserving, and sparsity, *i.e.* the observation that only a few materials contribute to the reflectance even when the sample consists of multiple component materials.

Tongbuasirilai et al. (2022) developed a sparse BRDF model using basis functions, which they referred to as dictionaries. They use machine learning to reduce the 4D BRDF space into sparse coefficients describing the reflectance profile. Two databases were used, the MERL 100 and the parametric modeled database developed by Dupuy and Jacob. The fit or compression of the basis functions into coefficients is largely determined by the reflectance, with shinier materials requiring more coefficients. The best basis is selected from a training set of 32 basis functions, which has the sparsest coefficients and the most signal to noise fidelity. Ultimately, the ideal candidate is selected from a reduced set by rendering images of the models using image metrics similar to Bieron and Peers, as previously described. Tongbuasirilai et al. (2022) consider this approach more flexible and descriptive than separation by the diffuse and specular components. The research also demonstrated that two such models can be interpolated to form an intermediary BRDF using the model's sparse coefficients which has reflectance from both models.

Recent advancements in data driven fitting include a neural network to establish the fit or extract the key components. Given the BRDF is itself a weighting of specular and diffuse reflection, fitting within a network of consisting of weights and biases is a sound, and logical approach. A key technique uses an auto-encoder as the type of network. This type of network is trained to feed the output back into the input layer, learning to minimize the error by comparing the input and output data points whilst compressing the data into a lower dimension, latent representation. Neural networks have a distinct advantage over other methods as they can capture phenomenon which is non-linear. The accuracy of the reconstruction of these neural BRDFs (nBRDF) is therefore improved. Hu et al. (2020) and a similar study by Sztrajman et al. (2021) compressed BRDFs in a lightweight auto-encoder network. One of the key differences was Hu, et al. decoded to tabulated data for rendering, whereas the later study by Sztrajman, et al. included the ability to use the compressed nBRDF directly in a rendering system, with the neural network acting as the decoder at rendering speed comparable to an analytical model. The MERL 100 dataset was used in an 80% training – 20% testing scheme, and took permutations of the RGB channels to compensate for the low pool of material for training. The training stage essentially aims to compute a cost function between predicted data and the measured material. For this cost function, the logarithmic loss applied to cosine weighted reflectance values was used. The training scheme leveraged importance direction sampling, with two hidden network layers, and extrapolated to 32 components. Anisotropic materials were also considered, although the fit showed a higher structural similarity index metric error than isotropic materials. Interpolation between two distinct materials was also demonstrated via interpolation of the latent basis components between the two materials.

Neural networks have also been demonstrated on BTF data. The amount of data generated for BTF measurements is significant and a problem exists gathering enough angular data. The interpolation between samples is a lossy process or the memory footprint is too immense to store sufficient samples. Additionally, matrix factorization techniques, like principal component analysis (PCA), assume a

linear dependence and therefore miss non-linear dependencies. Rainer et al. (2019) instead use an auto-encoder network to extract latent features from the textures representing the angular light and view directions. The training data was taken from the University of Bonn BTF dataset mentioned in *Section 3.5*. Additionally, two textile materials were measured which exhibited angular color dependence, an important test case for view-dependent reflectance evaluation. These were measured on a custom 4 axis gonio-reflectometer, similar in design to those mentioned in *Section 3.2*. The training scheme was a numeric  $L_2$  loss between input and output pairs, and the network consisted of 4 hidden layers, trained for 400 epochs. A simple, high frequency decoder was designed to query each texel for the light and view direction and output a corresponding RGB vector. Most rendering algorithms adopt a similar texel query method to efficiently evaluate reflectance. The compression ratio of the technique was observed to be twice as efficient as PCA. Acceptable rendering times comparable to existing methods were observed.

### 3.3 Hybridized Approaches

A hybrid fitting approach takes a combination of non-parametric basis functions and parametric approaches. Bagher et al. (2016), for example, developed a non-parametric fitting technique for isotropic materials which uses the micro-faceted model as the basis functions, termed “non-parametric factored microfacet model.” It can be efficiently compressed to 3.2KB per material, while the measured MERL database materials are 33 Mb per material. Fits were made from the MERL database using three tabulated factors for the  $D$  (NDF),  $G$  (shadowing), and  $F$  (Fresnel) terms. Sun et al. (2018) developed a new fitting technique that separates the diffuse and specular components of the material under investigation using a partial image-based metric. This is a three-step algorithm which averages the reflectance across the color channels, which they refer to as the achromatic shape, by approximating the shape with an analytical model. It is stated that Lambertian distribution is preferred for the diffuse component over the more complex Oren and Nayer model shown in Table 1-2, and GGX is used for the specular component. The algorithm then refines the fit based on analytical approximations, *i.e.* the log and cubic root approximations, using PSNR analysis. Finally, the color is restored in the hue saturation intensity color space by using an image-based comparison metric, as it was found to outperform a BRDF-based metric. Separation of the diffuse and specular parts allows for novel editing of the measured data, such as changing the color of the BRDF or exchanging diffuse and specular components from different materials. Some limitations exist with multi-layer materials and materials that may exhibit some non-trivial subsurface scattering. It was also found that single reflectance lobes fail to capture the specularity of the material and two analytical BRDFs are instead used to construct the specular component.

## 4. CONCLUSION

In this paper, we explored the fundamental considerations for reflectance material rendering, including energy conservation, micro-facet distribution, and the analytic parameters of the BRDF model. We also discussed some problems related to representation, such as assumptions about the distribution model and approximations of the distribution itself. Furthermore, we reviewed the state-of-the-art in reflectance capture, and noted that there is still no clear standard for measuring bidirectional reflectance distribution. We observed that while many novel and creative solutions have been proposed, no device can capture all the dimensions required to recreate the complete scattering function. Moreover, high-density spectral resolution and anisotropic measurements are under-represented in publicly available datasets, despite being necessary for accurate rendering.

We provided examples of how micro-facet parameters are evaluated against real measured data and incorporated into commercial renderers. We also examined different approaches to data fitting, including fitting existing analytical models to the data using metrics, starting with the data and using an inverse strategy, and hybrid approaches. Finally, we suggested that newer neural network approaches

may offer advantages over linear factorization techniques by capturing non-linear dependencies while retaining a compact representation.

### **CONFLICT OF INTEREST**

The authors declare no conflict of interest.

### **ACKNOWLEDGMENT**

The Commonwealth of Australia (represented by the Defence Science and Technology Group) supported this research through a Defence Science Partnerships agreement. Belinda Tepper would like to acknowledge the Research Scholarship provided by the Defence Science and Technology Group and the Australian Government Research Training Program (RTP).

## REFERENCES

- Akenine-Moller, T., Haines, E., & Hoffman, N. (2008). Real-Time Rendering (3rd ed.). A K Peters/CRC Press. doi:10.1201/9781315365459
- Ashikhmin, M., Premoze, S., & Shirley, P. (2000). A microfacet-based BRDF generator. *Proceedings of the 27th annual conference on computer graphics and interactive techniques*. doi:10.1080/10867651.2000.10487522
- Ashikhmin, M., & Shirley, P. (2000). An Anisotropic Phong BRDF Model. *Journal of Graphics Tools*, 5(2), 25–32. doi:10.1080/10867651.2000.10487522
- Baek, S.-H., Zeltner, T., Ku, H. J., Hwang, I., Tong, X., Jakob, W., & Kim, M. H. (2020). Image-Based Acquisition and Modeling of Polarimetric Reflectance. *ACM Transactions on Graphics*, 39(4). Advance online publication. doi:10.1145/3386569.3392387
- Bagher, M. M., Snyder, J., & Nowrouzezahrai, D. (2016). A Non-Parametric Factor Microfacet Model for Isotropic BRDFs. *ACM Transactions on Graphics*, 35(5), 1–16. Advance online publication. doi:10.1145/2907941
- Baribeau, R., Neil, W. S., & Côté, É. (2009). Development of a robot-based gonioreflectometer for spectral BRDF measurement. *Journal of Modern Optics*, 56(13), 1497–1503. doi:10.1080/09500340903045702
- Bieron, J., & Peers, P. (2020). An Adaptive BRDF Fitting Metric. *Computer Graphics Forum*, 39(4), 59–74. doi:10.1111/cgf.14054
- Blinn, J. F. (1977). Models of Light Reflection for Computer Synthesized Pictures. *SIGGRAPH Comput. Graph.*, 11(2), 192–198, 197. doi:10.1145/965141.563893
- Burley, B. (2012). Physically-Based Shading at Disney. In SIGGRAPH Course: Practical physically-based shading in film and game production. ACM
- Cook, R. L. (1984). Shade Trees *Proceedings of the 11th Annual Conference on Computer Graphics and Interactive Techniques*. doi:10.1145/800031.808602
- Cook, R. L., & Torrance, K. E. (1982). A Reflectance Model for Computer Graphics. *ACM Transactions on Graphics*, 1(1), 7–24. Advance online publication. doi:10.1145/357290.357293
- Dana, K., Ginneken, B., Nayar, S., & Koenderink, J. (1999). Reflectance and texture of real-world surfaces. *ACM Transactions on Graphics*, 18(1), 1–34. doi:10.1145/300776.300778
- Dupuy, J., & Jakob, W. (2018). An adaptive parameterization for efficient material acquisition and rendering. *ACM Transactions on Graphics*, 37(6), 1–14. doi:10.1145/3272127.3275059
- Filip, J., & Vávra, R. (2014). Template-Based Sampling of Anisotropic BRDFs. *Computer Graphics Forum*, 33(7), 91–99. doi:10.1111/cgf.12477
- Filip, J., Vávra, R., Haindl, M., Zid, P., Krupika, M., & Havran, V. (2013). BRDF slices: Accurate adaptive anisotropic appearance acquisition. *Proceedings of the IEEE Conference on Computer Vision and Pattern Recognition*. [https://openaccess.thecvf.com/content\\_cvpr\\_2013/html/Filip\\_BRDF\\_Slices\\_Accurate\\_2013\\_CVPR\\_paper.html](https://openaccess.thecvf.com/content_cvpr_2013/html/Filip_BRDF_Slices_Accurate_2013_CVPR_paper.html)
- Forés, A., Ferwerda, J., & Gu, J. (2012). Toward a perceptually based metric for BRDF modeling. *Final Program and Proceedings - IS and T/SID Color Imaging Conference, CIC'12*, 142–148.
- Heitz, E. (2014). Understanding the masking-shadowing function in microfacet-based BRDFs. *Journal of Computer Graphics Techniques*, 3(2), 32–91.
- Holroyd, M., Lawrence, J., & Zickler, T. (2010). A coaxial optical scanner for synchronous acquisition of 3D geometry and surface reflectance. *ACM Transactions on Graphics*, 29(4), 1–12. doi:10.1145/1778765.1778836
- Hu, B., Guo, J., Chen, Y., Li, M., & Guo, Y. (2020). DeepBRDF: A Deep Representation for Manipulating Measured BRDF. *Computer Graphics Forum*, 39(2), 157–166. doi:10.1111/cgf.13920
- Jensen, H. W., Marschner, S. R., Levoy, M., & Hanrahan, P. (2001). A practical model for subsurface light transport. *Proceedings of the 28th annual conference on computer graphics and interactive techniques*. doi:10.1145/383259.383319

- Karis, B. (2013). Real shading in unreal engine 4. *Proc. Physically Based Shading Theory Practice*, 4(3). doi:10.1145/383259.383319
- Lafortune, E. P. F., Foo, S.-C., Torrance, K. E., & Greenberg, D. P. (1997). Non-Linear Approximation of Reflectance Functions. *Proceedings of the 24th Annual Conference on Computer Graphics and Interactive Techniques*. doi:10.1145/258734.258801
- Lavoué, G., Bonneel, N., Farrugia, J.-P., & Soler, C. (2021). Perceptual quality of BRDF approximations: Dataset and metrics. *Computer Graphics Forum*, 40(2), 327–338. doi:10.1111/cgf.142636
- Lawrence, J., Ben-Artzi, A., DeCoro, C., Matusik, W., Pfister, H., Ramamoorthi, R., & Rusinkiewicz, S. (2006). Inverse Shade Trees for Non-Parametric Material Representation and Editing. *ACM Transactions on Graphics*, 25(3), 735–745. doi:10.1145/1141911.1141949
- Li, M., Zhou, Z., Wu, Z., Shi, B., Diao, C., & Tan, P. (2020). Multi-View Photometric Stereo: A Robust Solution and Benchmark Dataset for Spatially Varying Isotropic Materials. *IEEE Transactions on Image Processing*, 29, 1–1. doi:10.1109/TIP.2020.2968818 PMID:32011254
- Löw, J., Kronander, J., Ynnerman, A., & Unger, J. (2012). BRDF Models for Accurate and Efficient Rendering of Glossy Surfaces. *ACM Transactions on Graphics*, 31(1), 1–14. Advance online publication. doi:10.1145/2077341.2077350
- Lu, R., Koenderink, J., & Kappers, A. (2000). Optical Properties (Bidirectional Reflectance Distribution Function) of Shot Fabric. *Applied Optics*, 39(31), 5785–5795. doi:10.1364/AO.39.005785 PMID:18354579
- Lyngby, R. A., Matthiassen, J. B., Frisvad, J. R., Dahl, A. B., & Aanaes, H. (2019). Using a Robotic Arm for Measuring BRDFs. *Image Analysis: 21st Scandinavian Conference, SCIA 2019 Proceedings*. doi:10.1007/978-3-030-20205-7\_16
- Marschner, S., Westin, S., Lafortune, E., & Torrance, K. (2000). Image-Based Bidirectional Reflectance Distribution Function Measurement. *Applied Optics*, 39(16), 2592–2600. doi:10.1364/AO.39.002592 PMID:18345176
- Marschner, S. R., Jensen, H. W., Cammarano, M., Worley, S., & Hanrahan, P. (2003). Light scattering from human hair fibers. *ACM Transactions on Graphics*, 22(3), 780–791. doi:10.1145/882262.882345
- Marschner, S. R., Westin, S. H., Arbree, A., & Moon, J. T. (2005). Measuring and modeling the appearance of finished wood. In *ACM SIGGRAPH 2005 Papers* (pp. 727–734). doi:10.1145/1186822.1073254
- Matusik, W., Pfister, H., Brand, M., & McMillan, L. (2003). A Data-Driven Reflectance Model. *ACM Transactions on Graphics*, 22(3), 759–769. doi:10.1145/882262.882343
- Ngan, A., Durand, F., & Matusik, W. (2005). Experimental Analysis of BRDF Models. *Eurographics Symposium on Rendering*. doi:10.2312/EGWR/EGSR05/117-126
- Nguyen, H. (2008). *GPU Gems 3*. Addison-Wesley. <https://books.google.com.au/books?id=yINyQgAACAAJ>
- Nicodemus, F. E., Richmond, J. C., Hsia, J. J., Ginsberg, I. W., Limperis, T., Harman, S., & Baruch, J. J. (1977). *Geometrical considerations and nomenclature for reflectance*. <https://api.semanticscholar.org/CorpusID:18645782>
- Oren, M., & Nayar, S. K. (1994). Generalization of Lambert's Reflectance Model. *Proceedings of the 21st Annual Conference on Computer Graphics and Interactive Techniques*. doi:10.1145/192161.192213
- Öztürk, A., Kurt, M., & Bilgili, A. (2010). A Copula-Based BRDF Model. *Computer Graphics Forum*, 29(6), 1795–1806. doi:10.1111/j.1467-8659.2010.01649.x
- Phong, B. T. (1975). Illumination for computer generated pictures. *Communications of the ACM*, 18(6), 311–317. doi:10.1145/360825.360839
- Rainer, G., Jakob, W., Ghosh, A., & Weyrich, T. (2019). Neural BTF Compression and Interpolation. *Computer Graphics Forum*, 38(2), 235–244. doi:10.1111/cgf.13633
- Rusinkiewicz, S. (1997). A survey of brdf representation for computer graphics. Tech. rep. Princeton University.

- Rusinkiewicz, S. M. (2011). A New Change of Variables for Efficient BRDF Representation. In *Rendering Techniques '98* (pp. 11–22). Springer Vienna.
- Sandmeier, S. R., & Itten, K. I. (1999). A field goniometer system (FIGOS) for acquisition of hyperspectral BRDF data. *IEEE Transactions on Geoscience and Remote Sensing*, *37*(2), 978–986. doi:10.1109/36.752216
- Schlick, C. (1994). An Inexpensive BRDF Model for Physically-based Rendering. *Computer Graphics Forum*, *13*(3), 233–246. doi:10.1111/1467-8659.1330233
- Schröder, K., Zhao, S., & Zinke, A. (2012). Recent advances in physically-based appearance modeling of cloth. *SIGGRAPH Asia 2012 Courses, SA 2012*. doi:10.3390/s140507753
- Schwartz, C., Sarlette, R., Weinmann, M., Rump, M., & Klein, R. (2014). Design and Implementation of Practical Bidirectional Texture Function Measurement Devices Focusing on the Developments at the University of Bonn. *Sensors (Basel)*, *14*, 7753–7819. doi:10.3390/s140507753
- Soldado, R. M., & Almagro, C. U. (2012). *An Overview of BRDF Models*. <https://api.semanticscholar.org/CorpusID:44900609>
- Sun, T., Jensen, H. W., & Ramamoorthi, R. (2018). Connecting measured brdfs to analytic brdfs by data-driven diffuse-specular separation. *ACM Transactions on Graphics*, *37*(6), 1–15. doi:10.1145/3272127.3275026
- Sztrajman, A., Rainer, G., Ritschel, T., & Weyrich, T. (2021). Neural BRDF Representation and Importance Sampling. *Computer Graphics Forum*, *40*(6), 332–346. doi:10.1111/cgf.14335
- Tongbuasirilai, T., Unger, J., Guillemot, C., & Miandji, E. (2022). A Sparse Non-Parametric BRDF Model. *ACM Transactions on Graphics*, *41*(5), 1–18. Advance online publication. doi:10.1145/3533427
- Ward, G. J. (1992). Measuring and Modeling Anisotropic Reflection. *Computer Graphics*, *26*(2), 265–272. doi:10.1145/142920.134078
- Weinmann, M., Gall, J., & Klein, R. (2014, September). Material Classification Based on Training Data Synthesized Using a BTF Database. *European Conference on Computer Vision*. doi:10.1145/1401132.1401234
- Weyrich, T., Lawrence, J., Lensch, H., Rusinkiewicz, S., & Zickler, T. (2009). Principles of Appearance Acquisition and Representation. *Foundations and Trends in Computer Graphics and Vision*, *4*, 75–191. doi:10.1145/1401132.1401234
- Whitted, T. (1980). An improved illumination model for shaded display. *Communications of the ACM*, *23*(6), 343–349. doi:10.1145/358876.358882
- Wu, K., & Yuksel, C. (2017). Real-Time Cloth Rendering with Fiber-Level Detail. *IEEE Transactions on Visualization and Computer Graphics*, 1–1. doi:10.1109/TVCG.2017.2731949 PMID:28749354
- Yang, S. K., Song, I.-U., Oh, E., Yang, H.-S., & Kim, S.-W. (2020). Development of a new image based BRDF measurement system using a semicircular ring. *Reflection, Scattering, and Diffraction from Surfaces VII*.

## ENDNOTE

- <sup>1</sup> The screen door effect is the result of the imperfect coverage of pixels at the micro-scale. In a magnification scenario, such as a projection, the borders surrounding the pixels become observable and resemble a screen door.